Supplementary Information:

I. Material characterization

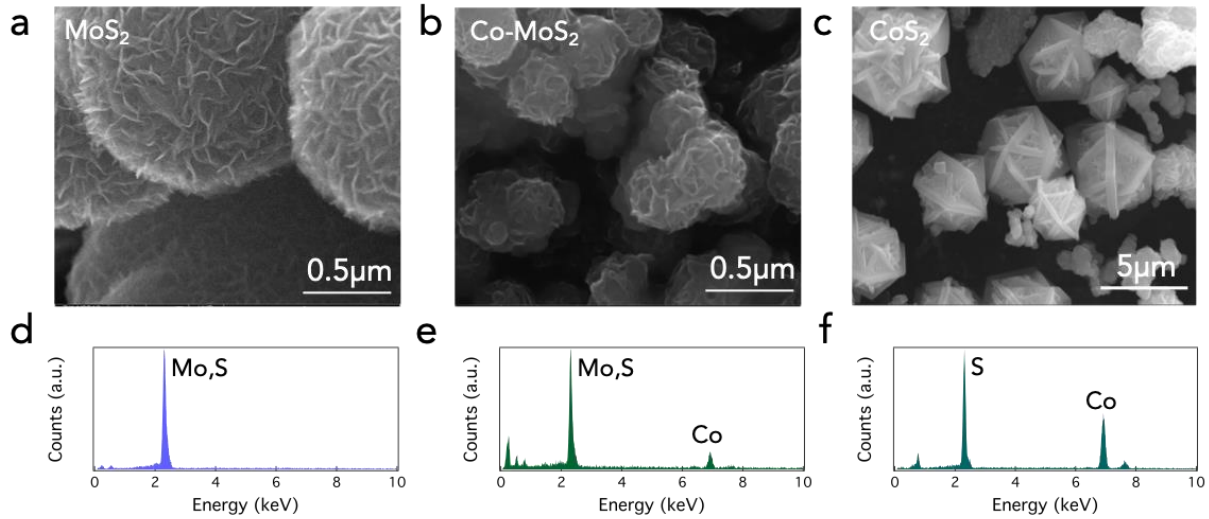

Figure S1. SEM images and corresponding EDAX of (a)(d) MoS_{2-x} (b)(e) Co-doped MoS_{2-x} and (c)(f) CoS_2.

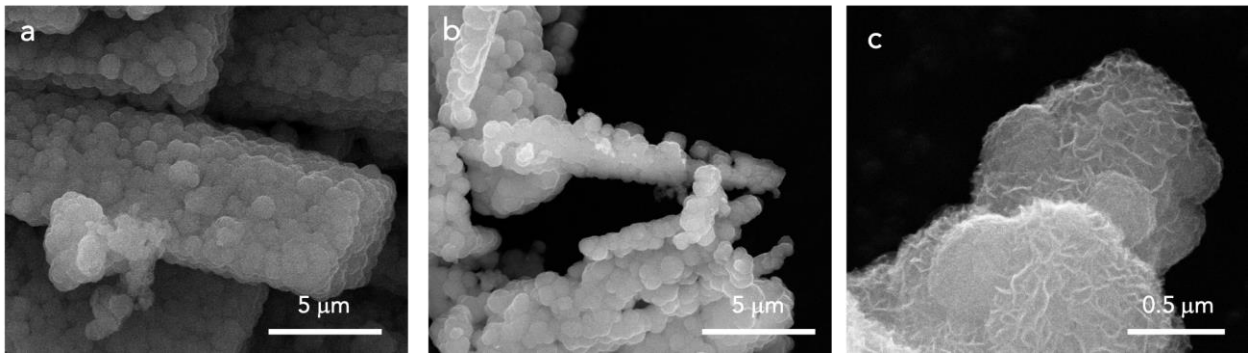

Figure S2. SEM image of hydrothermal samples synthesized from precursor recipe of 1:9 Co/Mo molar ratio. Spheres made of MoS_{2-x} nanosheets assembles into bars (a) and plates (b), entirely different from the morphology shown in Figure S1b. The shapes of the spheres are turning into hexagons, resembling the morphology of CoS_2 shown in Figure S1c. (b) Magnified morphology of MoS_{2-x} spheres in (a), showing MoS_{2-x} covering those spheres. The morphology evolution at 1:9 Co/Mo molar ratio implies a possible Co_xS_y/Co-dope MoS_{2-x} phase separation process.

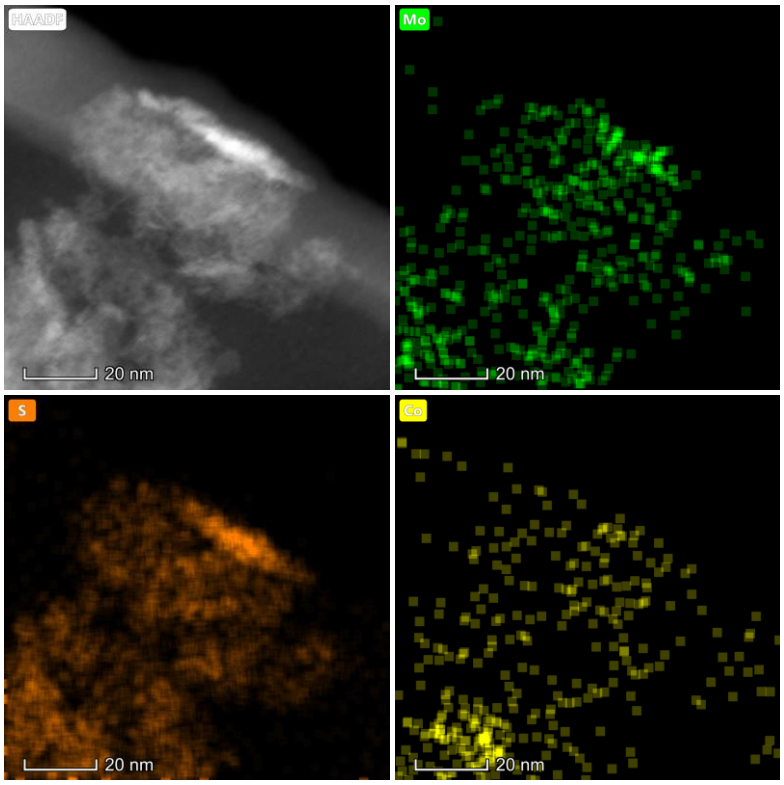

Figure S3. Additional EDAX mapping on Co-doped MoS_{2-x}.

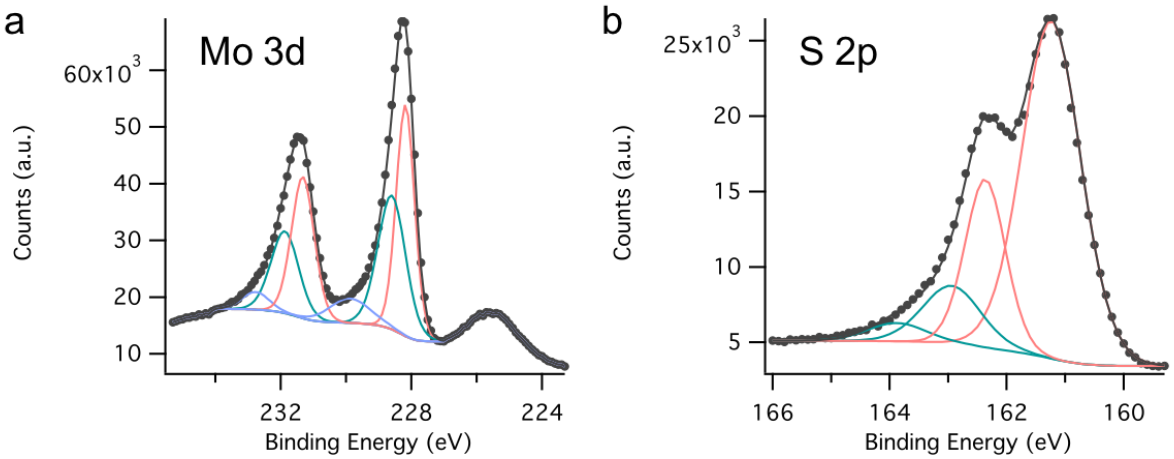

Figure S4. XPS spectra of un-doped MoS_{2-x} grown by hydrothermal method.

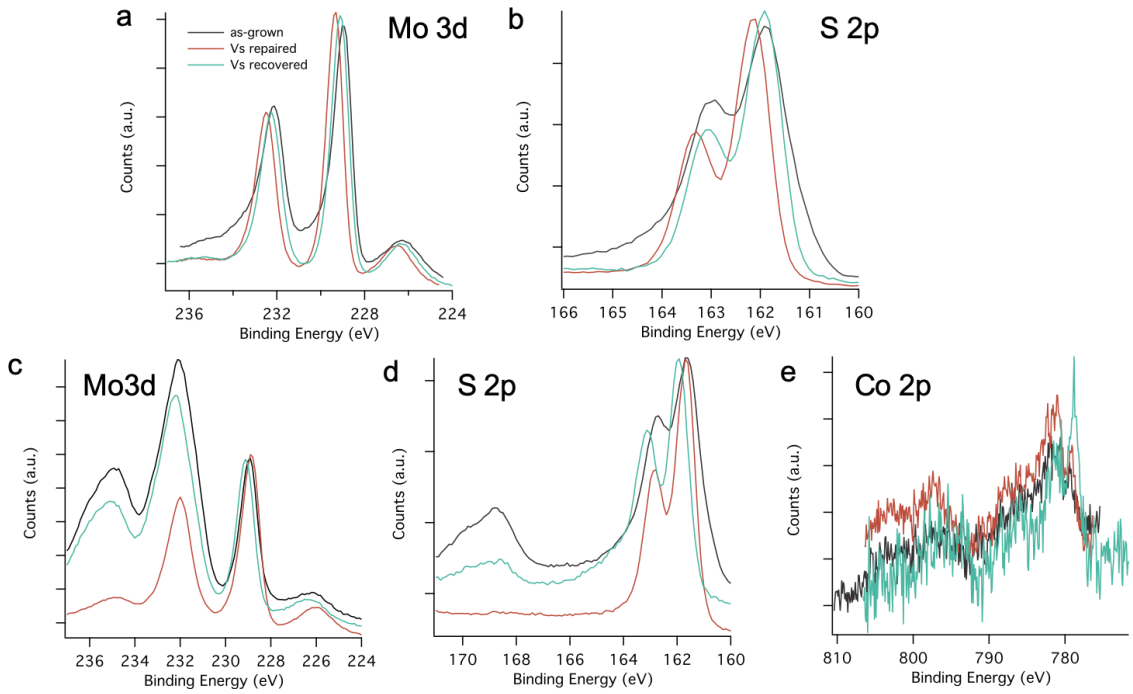

Figure S5. XPS of V_S-repaired and V_S-recovered MoS_{2-x} and Co-MoS_{2-x}.

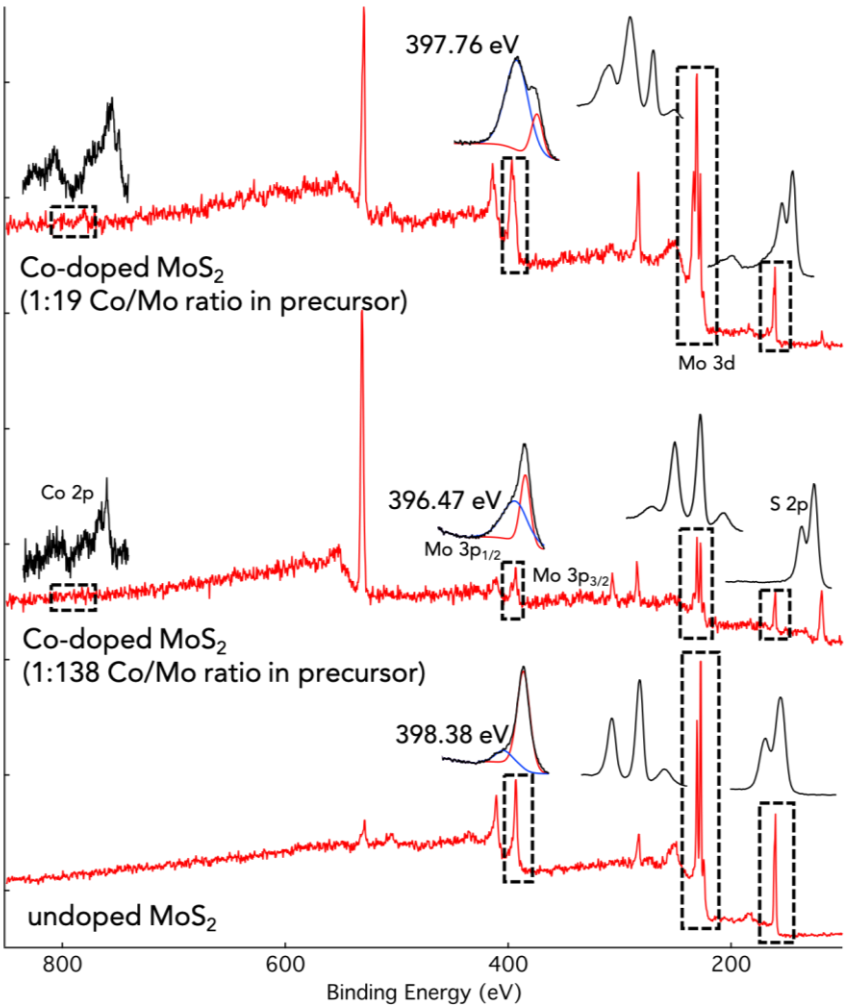

Figure S6. XPS of undoped and Co-doped MoS_{2-x} samples.

Table S1. Calculated S/Mo ratio from XPS.

	un-doped	Co-doped
as-grown	1.85	1.39
S annealed	1.92	1.54
N_2H_4 treated	1.88	1.45

Table S2. Calculated Co doping concentration from XPS.

	Co/(Co+Mo)
as-grown	6.38%
S annealed	6.47%
N_2H_4 treated	5.49%

XPS analysis:

The XPS signal of undoped MoS_{2-x} synthesized by hydrothermal method is presented in Figure S4. The peaks of Mo 3d core level is deconvoluted into three sets of signals. Two of them (red and green) are prominent, assigned to Mo in original (without S vacancy) and defected MoS_{2-x} structures (with S vacancy), respectively. Accordingly, the peaks S 2p core level is deconvoluted into two corresponding sets of signals. The blue curve implies some other Mo state accompanied with multiple S vacancies.

The XPS signal of Co-doped MoS_{2-x} synthesized by hydrothermal method is presented in Figure 2c. The peaks of Mo 3d core level is deconvoluted into four sets of signals. Two of them (yellow and green) are similar to the peaks in undoped MoS_{2-x}. The other two (blue and red) are assigned to Mo next to Co dopant without and with S vacancy, respectively. Notably, the signal of Mo not accompanied with Co dopant, but with S vacancy (green in Figure S4a and Figure 2c) is significantly suppressed after Co doping, implying the tendency of S vacancy to simultaneously form close to Co dopant. Accordingly, the peaks of S 2p core level is perfectly deconvoluted into three sets of signals, without one assigned to the S vacancy far from a Co dopant.

Figure S5 displays the effect of S vacancy repair and recovery on the XPS core levels. In both undoped and Co-doped cases, Vs repair makes the 'valley' between the neighbor peaks of Mo and S core levels deeper (black to red), indicating less convoluted of the overall signal and suppression of the S vacancy related signals. As discussed in the main text, hydrazine treatment recovers S vacancy to limited extent, proved by the evolution from red to green curves, showing signs of reversion to the black curve, but not fully. The peaks related to Co doping (as mentioned in the discussion for Figure 2c) are significantly suppressed after Vs repair, and strengthened after Vs recovery, showing their strong correlation.

All our analysis of the XPS deconvolution matches the data in the reference,[1] i.e. Mo 3d5/2: 228 ~ 233 eV, S 2p3/2: 160 ~ 178 eV.

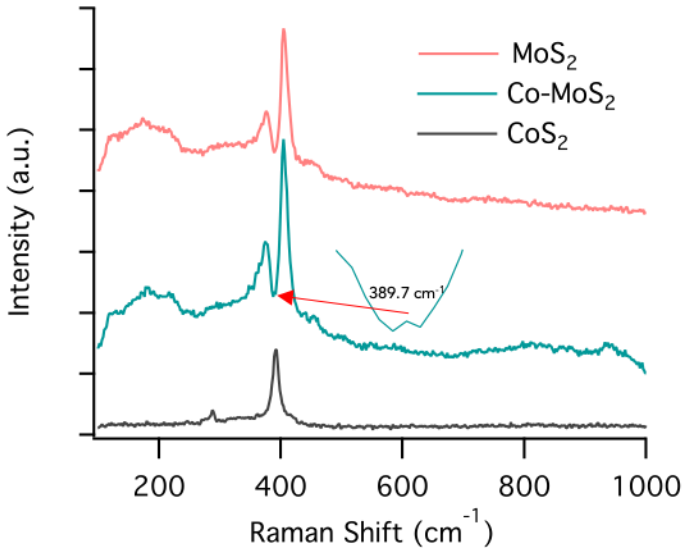

Figure S7. Raman spectra of MoS_{2-x}, Co-doped MoS_{2-x} and CoS_2. The broad peaks around 200 cm^{-1} are possibly defect related. The spectra are identical except for the tiny peak near 390 cm^{-1} for Co-MoS_{2-x}.

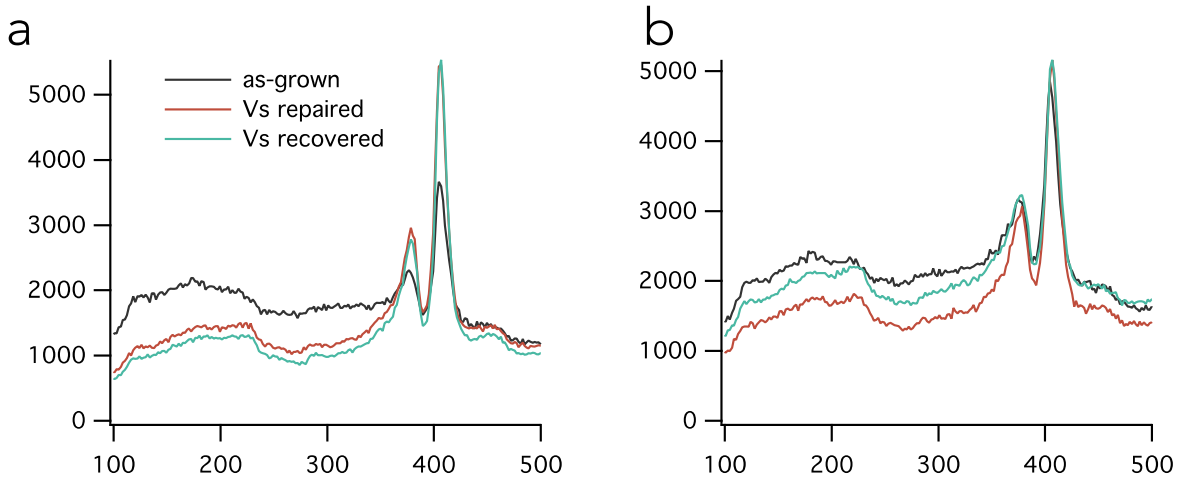

Figure S8. Raman of V_S-repaired and V_S-recovered MoS_{2-x} (a) and Co-MoS_{2-x} (b).

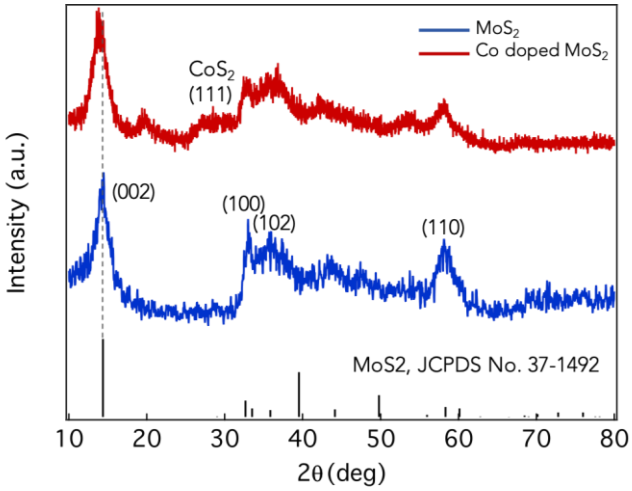

Figure S9. X-ray diffraction pattern of undoped and Co-doped MoS_{2-x}.

II. DFT calculation

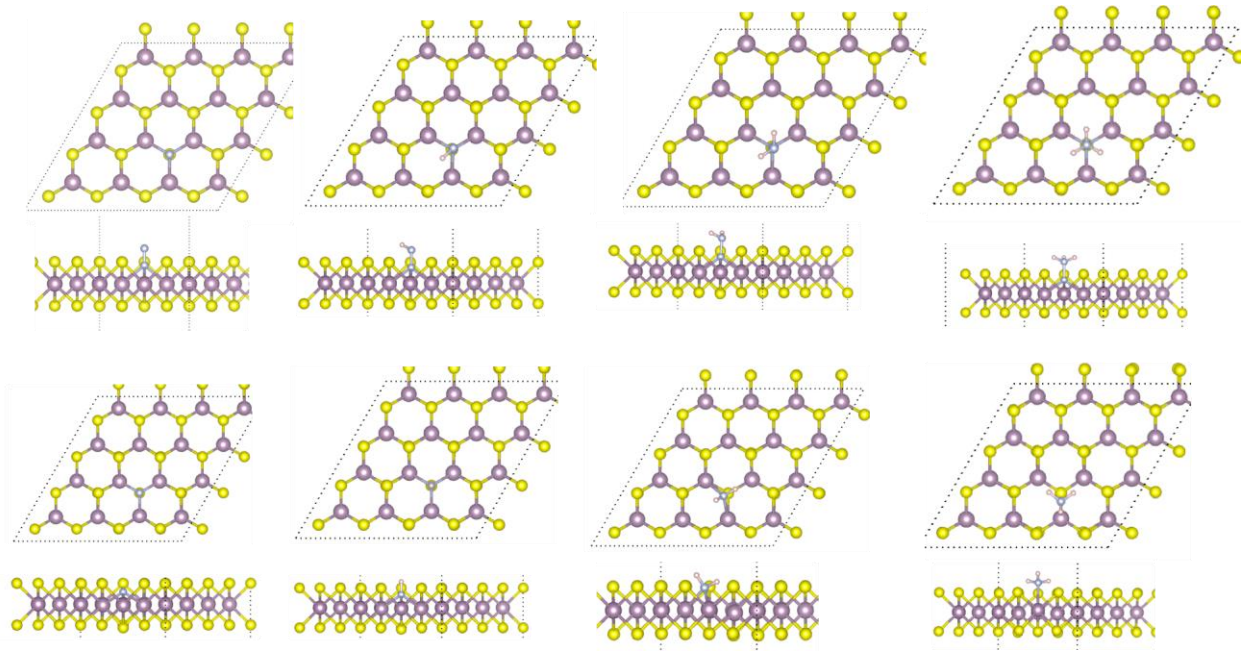

Figure S10. Top-view and side-view of relaxed structures of MoS_2 with single V_s in a 4×4 unit cell for each step of the ammonia production. Purple yellow, grey and pink spheres represent molybdenum, sulfur, nitrogen and hydrogen, respectively.

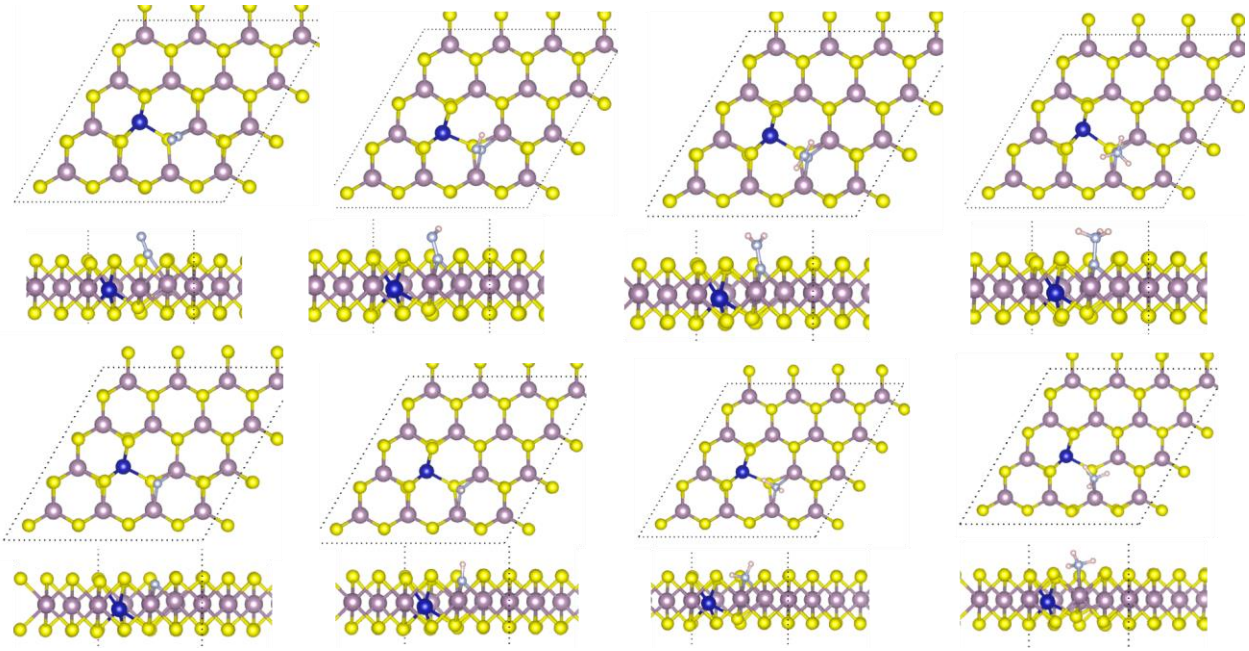

Figure S11. Top-view and side-view of relaxed structures of Co-doped MoS_2 with single V_s in a 4×4 unit cell for each step of the ammonia production. Blue spheres represent cobalt.

III. NRR characterization

NRR parameters calculation:

Assuming the amount of ammonia N determined by chromogenic method is n_N, total amount of charge during the reaction determined by integration of i-t curve is Q, the reaction time is t, the

weight of catalyst loaded on the carbon cloth is m_{cata}, the charge of an electron is e, Avogadro's constant is N, the production rate and Faradaic efficiency is calculated as follows:

$$r_{production} = \frac{n_N}{m_{cata} * t}$$

$$\eta_{Faradic} = \frac{3 * e * N * n_N}{Q}$$

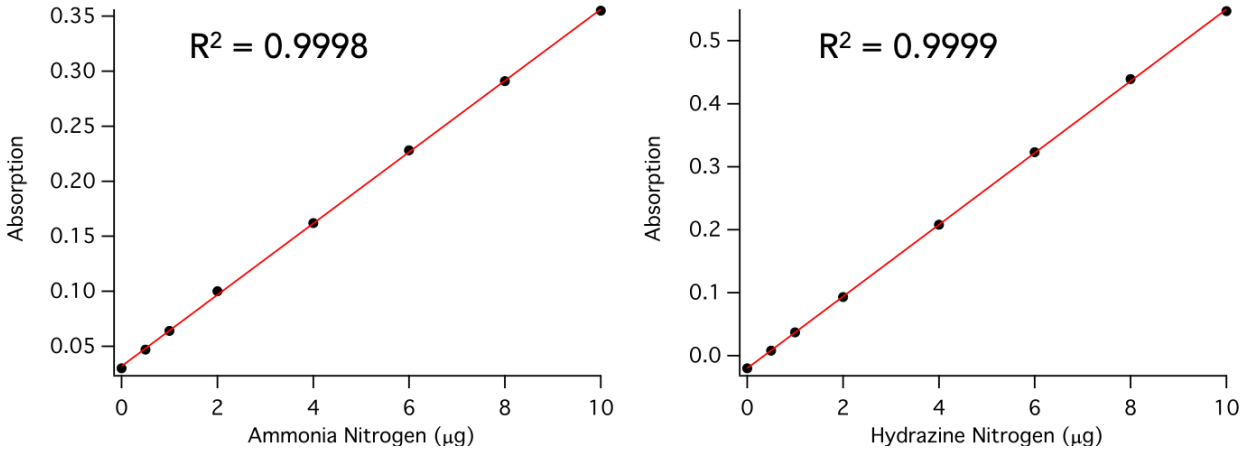

Figure S12. Calibration curves of ammonia nitrogen and hydrazine nitrogen.

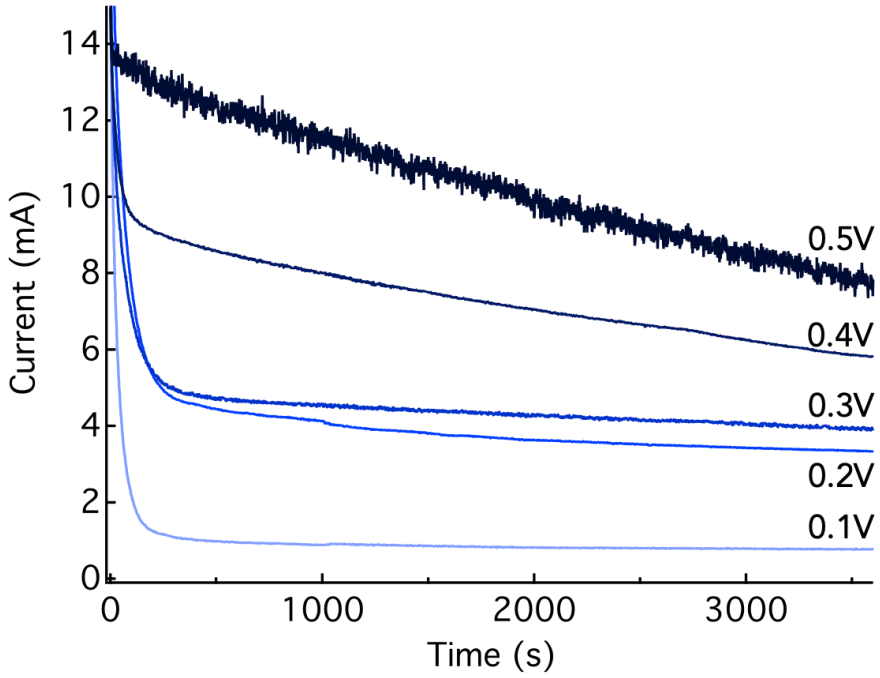

Figure S13. I-t curve of NRR tests at elevated overpotentials.

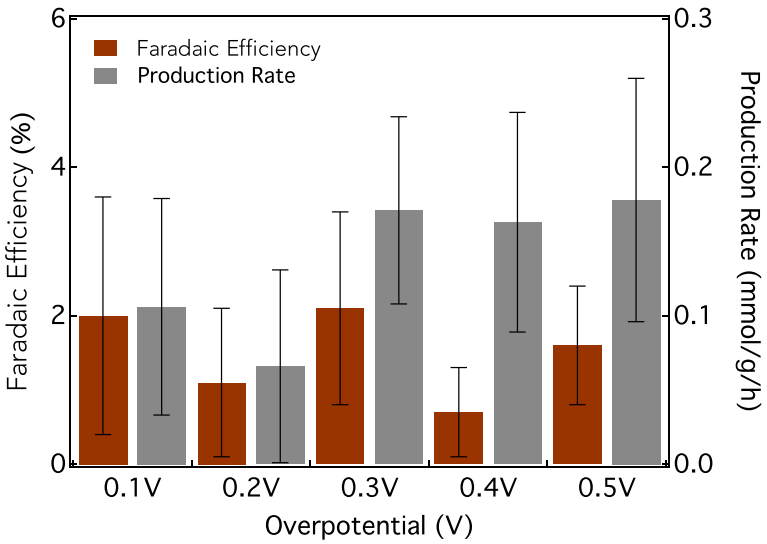

Figure S14. Dependence of hydrazine production on overpotentials.

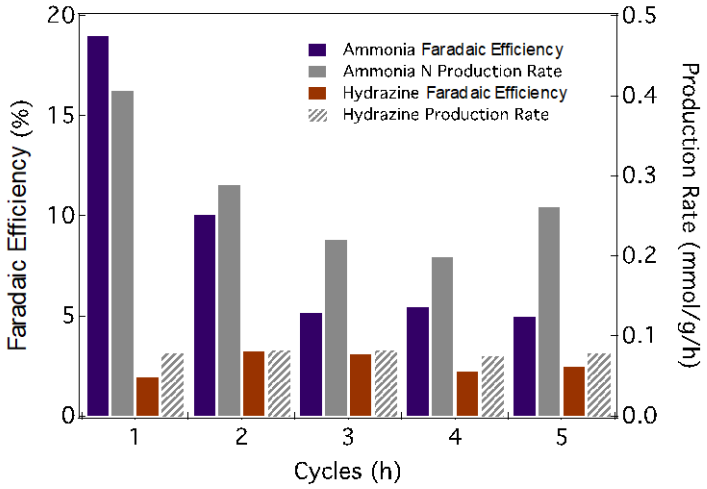

Figure S15. Cyclic tests for ammonia nitrogen and hydrazine at 0.3 V overpotential. Both Faradaic efficiency and production rate drops in the first two cycles and reaches a steady state in the following cycles. Considering it is reduction bias applied during the reaction and MoS_2 is electrochemically stable in the bias range, we attribute the degrade of the overall performance to the following reason: as a layered material, Co-doped MoS_{2-x} suffers from delamination with hydrogen evolution accompanied with NRR. Decreased amount of loaded MoS_{2-x} will certainly lead to degraded production rate. Faradaic efficiency, which should remain constant for the material, degrades as well because delamination of MoS_{2-x} will expose carbon cloth, and the latter is known to moderately catalyze hydrogen evolution but poorly do NRR reaction.[2, 3]

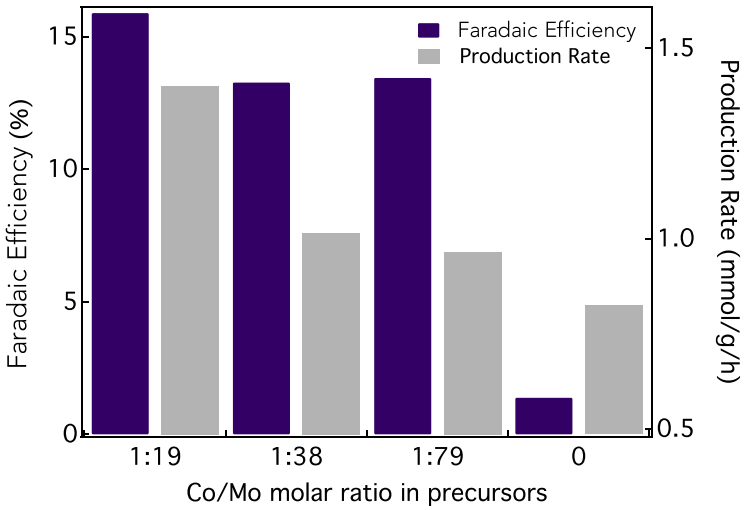

Figure S16. Dependence of Faradaic efficiency and production rate on the Co/Mo molar ratio in hydrothermal precursors.

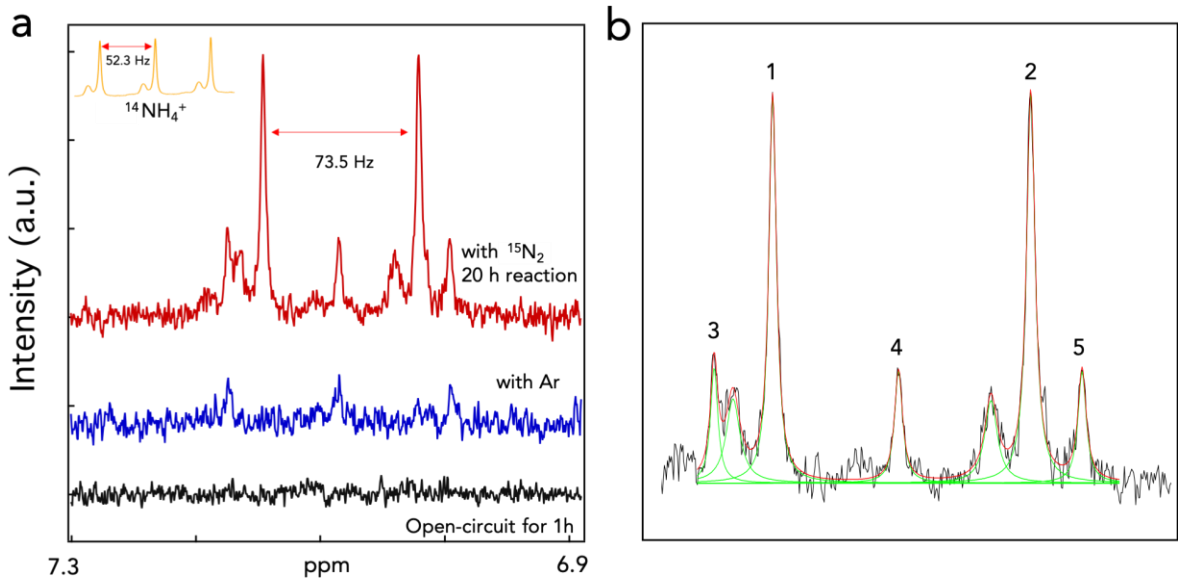

Figure S17. (a) NMR spectra of samples derived from ^{15}N labeled N_2 (red curve). The inset (yellow) curve shows the NMR pattern for ^{14}N NH_4^+. (b) Deconvoluted peaks of red curve in (a). Peak 1, 2 and 3, 4, 5 correspond to ^{15}N and ^{14}N ammonia detected from the NMR test, respectively. The ^{15}N ammonia percentage in the overall product calculated from the integral areas of proton NMR peaks corresponding to ^{15}N and ^{14}N ammonia is 70%.

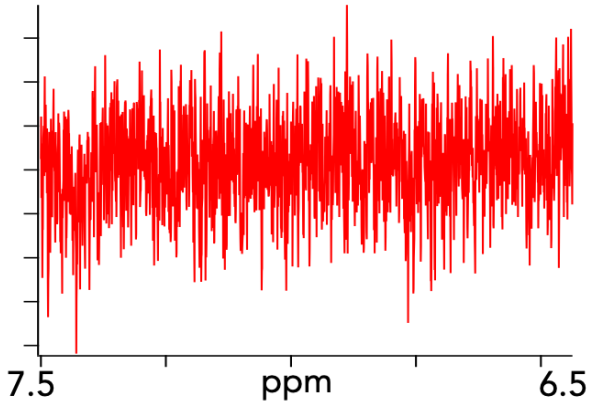

Figure S18. NMR spectra of solution with Co-doped MoS_{2-x} after ultrasonication in H_2SO_4 for 30 min.

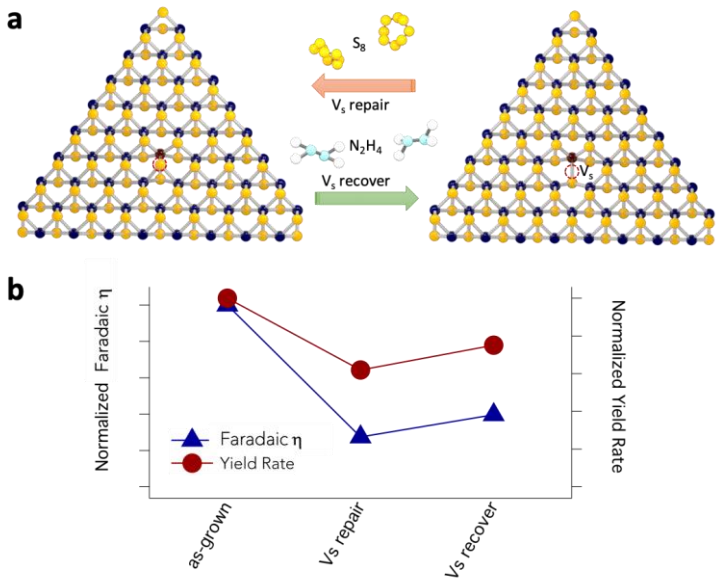

Figure S19. NRR performance modulated by defect repair and creation. (a) Schematic illustration of the S vacancy repair and recovery process *via* annealing in gaseous S atmosphere and treatment with hydrazine solution. (b) NRR performance evolution with S vacancy elimination and creation.

Table S3. Data for Figure S19b.

	Faradaic Efficiency (%)	Production Rate (mmol/g/h)
as-grown	10.21	0.822
S annealed	2.8	0.509
N_2H_4 treated	4.05	0.617

References:

1. Briggs, D., *Handbook of X-Ray and Ultraviolet Photoelectron Spectroscopy*. Heyden London: 1977.
2. Wen, L.; Yu, J.; Xing, C.; Liu, D.; Lyu, X.; Cai, W.; Li, X., Flexible Vanadium-Doped Ni 2 P Nanosheet Arrays Grown on Carbon Cloth for an Efficient Hydrogen Evolution Reaction. *Nanoscale* **2019**, *11*, 4198-4203.
3. Li, W.; Wu, T.; Zhang, S.; Liu, Y.; Zhao, C.; Liu, G.; Wang, G.; Zhang, H.; Zhao, H., Nitrogen-Free Commercial Carbon Cloth with Rich Defects for Electrocatalytic Ammonia Synthesis under Ambient Conditions. *Chem. Commun.* **2018**, *54*, 11188-11191.